Published in final edited form as:
Magn Reson Med. 2010 January ; 63(1): 243–252. doi:10.1002/mrm.22192.

In Vivo Generalized Diffusion Tensor Imaging (GDTI) Using Higher-Order Tensors (HOT)

Chunlei Liu[1], **Sarah C. Mang**[2], and **Michael E. Moseley**[3]

[1]Brain Imaging and Analysis Center, Duke University, Durham, North Carolina, USA

[2]Section of Experimental MR of CNS, Department of Neuroradiology, University Hospital Tuebingen, Tuebingen, Germany

[3]Lucas Center for MR Spectroscopy and Imaging, Department of Radiology, Stanford University, Stanford, California, USA

Abstract

Generalized diffusion tensor imaging (GDTI) using higher order tensor statistics (HOT) generalizes the technique of diffusion tensor imaging (DTI) by including the effect of non-Gaussian diffusion on the signal of magnetic resonance imaging (MRI). In GDTI-HOT, the effect of non-Gaussian diffusion is characterized by higher order tensor statistics (i.e. the cumulant tensors or the moment tensors) such as the covariance matrix (the second-order cumulant tensor), the skewness tensor (the third-order cumulant tensor) and the kurtosis tensor (the fourth-order cumulant tensor) etc. Previously, Monte Carlo simulations have been applied to verify the validity of this technique in reconstructing complicated fiber structures. However, no *in vivo* implementation of GDTI-HOT has been reported. The primary goal of this study is to establish GDTI-HOT as a feasible *in vivo* technique for imaging non-Gaussian diffusion. We show that probability distribution function (PDF) of the molecular diffusion process can be measured *in vivo* with GDTI-HOT and be visualized with 3D glyphs. By comparing GDTI-HOT to fiber structures that are revealed by the highest resolution DWI possible *in vivo*, we show that the GDTI-HOT can accurately predict multiple fiber orientations within one white matter voxel. Furthermore, through bootstrap analysis we demonstrate that *in vivo* measurement of HOT elements is reproducible with a small statistical variation that is similar to that of DTI.

Keywords

magnetic resonance imaging; diffusion; diffusion-weighted imaging; diffusiontensor imaging; generalized diffusion-tensor image; non-Gaussian diffusion; cumulants

Introduction

Measurement of molecular diffusion in biologic tissues with magnetic resonance imaging (MRI) has provided a very powerful tool for studying tissue architecture *in vivo* and non-invasively (1). To infer the underlying structure typically requires some physical model of the diffusion process and the accuracy is consequently limited by the associated assumptions. The

Correspondence Address: Chunlei Liu, Ph.D., Brain Imaging and Analysis Center, Duke University School of Medicine, 2424 Erwin Road, Suite 501, Campus Box 2737, Durham, NC 27705, Phone: (919)681 4788, Fax: (919)681 7033, chunlei.liu@duke.edu.

The paper was partially presented in the 16th Scientific Meeting and Exhibition of the International Society of Magnetic Resonance of Medicine.

diffusion tensor model (2), as the corner stone of this field, relies on the assumption of Gaussian diffusion (3). The recent realization of non-Gaussian diffusion within tissues and the need for more accurate description of the diffusion processes have prompted a number of recent developments, such as q-space imaging (4,5), diffusion spectrum imaging (6,7), high angular resolution diffusion imaging (8,9), Q-ball imaging (10), and two generalized diffusion tensor imaging (GDTI) methods (11–13) among others. Although the two GDTI methods share the same name, they differ fundamentally from each other (14). Here on, all discussions pertaining GDTI are based on Liu et al (12).

The generalized diffusion tensor imaging (GDTI) using higher order tensor statistics (HOT) by Liu et al (11,12) proposes to quantitatively characterize general diffusion processes with a series of diffusion tensors of increasing orders. Each tensor order offers a well defined physical interpretation. By the definition of standard statistics terminology, the second order tensor means the second order cumulant (covariance matrix), the third order tensor means the third order cumulant (skewness tensor), and the fourth order tensor means the fourth order cumulant (kurtosis tensor) and so on so forth (12,15). It has been shown that DTI is a second order approximation of the HOT model by assuming that all tensors of orders higher than two are zero (11,12). Furthermore, the diffusion kurtosis imaging (DKI) by Jensen et al (16) published two years after the initial introduction of GDTI-HOT is essentially a GDTI-HOT approximation that keeps only even-order tensors up to the fourth order. This fourth-order approximation was initially demonstrated in (11).

Simulation studies have demonstrated high accuracy of diffusion characterization by using HOT. The improved accuracy has helped to resolve a number of simple crossing fiber structures. For example, in Monte Carlo simulations, it was shown that GDTI-HOT was able to reconstruct a single tube with square cross section, connecting tubes forming an X-shape and connecting tubes forming a Y-shape (12). Some recent works have explored the significance of the kurtosis (fourth order statistics) in quantifying biological tissue complexity (16,17). In general, it is believed that by incorporating higher order statistics of random molecular motion, diffusion MRI can provide more detailed and more accurate information of tissue microstructure.

In this paper, we will present a very first *in vivo* implementation of GDTI-HOT. Similar to DTI, GDTI-HOT is susceptible to image geometric distortion and eddy current distortion that are common in diffusion-weighted images. Reliable *in vivo* measurement of HOT has been difficult because of these distortions using conventional DWI acquisition techniques. Recent development of multi-shot acquisition and parallel imaging has significantly improved the image quality of DWI. In this study, we applied the self-navigated interleaved spiral (SNAILS) DWI for image acquisition. Even order diffusion tensors up to order six are measured. Odd-order tensors are not reported due to the possible contamination of motion-induced phase error (12). These higher order tensors provide more quantitative information about molecular motion, new foundations for visualization and potential useful biomarkers. We will establish a feasible protocol on a clinical MRI scanner. The primary goal is to evaluate GDTI-HOT as a feasible and meaningful technique for measuring higher order tensor statistics *in vivo*, by studying the consistency and the reproducibility of *in vivo* measured HOT.

Materials and Methods

Theory of GDTI-HOT

To incorporate the effect of non-Gaussian diffusion, the GDTI-HOT method generalizes the Fick's law to (11,12)

$$\frac{\partial C}{\partial t}=D^{(2)}_{kl}\nabla_{kl}C+D^{(3)}_{klm}\nabla_{klm}C+D^{(4)}_{klmn}\nabla_{klmn}C+\cdots. \quad (1)$$

Here C is particle concentration; the coefficient $D^{(n)}_{i_1 i_2 \cdots i_n}$ is an n-th order diffusion tensor, where the superscript n in parentheses indicates the order of the tensor, and the subscript indicates the coordinate. Here and throughout this discussion, index notation follows Einstein's summation rule: if an index appears twice in an expression, then summation over that index is implied.

Following Torrey's treatment of diffusion, one can include the generalized Fick's law in the Bloch equation and solve it for a spin echo sequence. The transverse magnetization in a diffusion-weighted spin echo sequence evaluates to (11,12)

$$m(b)=m(0)\exp\left(\sum_{n=2}^{\infty}(-j)^n D^{(n)}_{i_1 i_2 \cdots i_n} b^{(n)}_{i_1 i_2 \cdots i_n}\right), \quad (2)$$

where $m(0)$ and $m(b)$ are the transverse magnetization measured at the echo time (TE) in the absence and presence of diffusion gradients, respectively. j is the square root of −1. The elements of the diffusion-weighting tensor $b^{(n)}$ are (11,12)

$$b^{(n)}_{i_1 i_2 \cdots i_n}=\gamma^n G_{i_1} G_{i_2} \cdots G_{i_n} \delta^n \left(\Delta-\frac{n-1}{n+1}\delta\right). \quad (3)$$

Here, γ is the gyromagnetic ratio; G_i is the i-th component of the magnetic field gradient vector; δ is the duration of each gradient lobe and Δ is the separation time of the two diffusion gradients. This theory differs from the high-angular resolution diffusion imaging (HARDI) (9,18) in that GDTI-HOT describes the signal behavior in the complete 3D q-space, while HARDI measures and analyzes the surface structure of the diffusivity at a given spherical surface in the q-space.

The main purpose of GDTI-HOT is to characterize the statistical property of the diffusion process with MRI-measurable quantities. It has been shown that these higher order diffusion tensors are proportional to the cumulants of the probability density function (PDF) of the diffusion process. More specifically, the second order tensor corresponds to the second order cumulant (covariance tensor), the third order tensor corresponds to the third order cumulant (skewness tensor), the fourth order tensor corresponds to the fourth order cumulant (kurtosis tensor) and so on (11,12). Once the higher order diffusion tensors are measured, the corresponding higher order cumulants can be computed based on the following relationship:

$$Q^{(n)}_{i_1 i_2 \cdots i_n}=(-1)^n n! D^{(n)}_{i_1 i_2 \cdots i_n}\left(\Delta-\frac{n-1}{n+1}\delta\right). \quad (4)$$

Finally, the PDF itself can be computed using the Gram-Charlier series (11,12),

$$p(\mathbf{r})=\mathrm{N}\left(0, Q^{(2)}_{kl}\right)\left(1+\frac{Q^{(3)}_{klm}}{3!}H_{klm}(\mathbf{r})+\frac{Q^{(4)}_{klmn}}{4!}H_{klmn}(\mathbf{r})+\cdots\right), \quad (5)$$

where $\mathrm{N}\left(0, Q_{kl}^{(2)}\right)$ is the normal distribution with zero-mean and covariance matrix $Q_{kl}^{(2)}=2D_{kl}^{(2)}\Delta$, and $H\, i_1 i_2 \ldots i_n$ (**r**)is the *n*-th order Hermite tensor (19).

In Vivo GDTI-HOT Protocol and Visualization

Brain imaging of a healthy volunteer was performed on a 3.0T GE scanner (GE Signa, GE Healthcare, Waukesha, WI). The study was approved by the Institution Review Board of Stanford University, and written consent was obtained from the volunteer prior to the scan. The scanner is equipped with a maximum gradient of 50mT/m and a slew rate of 150 mT/m/ms. A custom-built small head coil with improved sensitivity was used for receiving MR signals. Diffusion weighted images were acquired with the self-navigated interleaved spiral (SNAILS) technique (20). The scan parameters were: FOV = 192mm, slice thickness = 3mm, number of slices = 26, TR = 2.5s, TE = 76ms, bandwidth (BW) = 125 kHz, and matrix size =64×64 resulting in an isotropic resolution of 3×3×3 mm^3. A total of two interleaves of variable-density spirals were used to collect **k**-space data. The oversampled center **k**-space data provided the navigation for motion-induced phase error. Diffusion-weighted images were acquired on a set of 21 diffusion encoding directions (21), which were shown to perform well for GDTI-HOT (22). The 21 diffusion directions were repeated for four b-values (500, 1000, 2000 and 3000 s/mm^2). A set of non-diffusion-weighted images were also acquired for each b-value. The scan time for this protocol was 7.3 minutes. For the purpose of bootstrapping study, the whole protocol was repeated seven times.

Images were reconstructed using a conjugate-gradient (CG) algorithm. The CG algorithm corrects motion artifacts that are present in all diffusion-weighted images (23). Although odd-order tensors can be measured using the phase of the signal and they are important for understanding the asymmetry property of the PDF, residual motion-induced phase errors in the diffusion-weighted images can severely corrupt the accuracy of the measurement. Currently, there is no effective technique for measuring the phase caused by asymmetric non-Gaussian diffusion. Therefore only even order tensors were estimated using a least-squares estimator with the consideration of Rician noise in the diffusion-weighted images. In other words, here we are interested in accurately characterizing the symmetrical property of the PDF. The measurement of the even-order tensors is completely independent of that of the odd-order tensors because the even-order tensors only rely on the magnitude of MR signal. Therefore, the accuracy of the measured even-order tensors is not affected. Although the sixth-order tensor can be measured with this protocol, the main purpose of this protocol is to provide a practical and reliable method for measuring HOT up to the fourth order with clinically feasible scan time. A brief comparison of the fourth-order approximation and the sixth-order approximation is provided using images acquired with this protocol. Throughout this paper, a fourth-order approximation is assumed unless stated explicitly otherwise.

The shape of PDF provides a representation of the underlying neural fiber structure. To visualize the geometric structure of PDF, a 3D PDF glyph is constructed and displayed for each voxel. A PDF glyph is a closed 3D surface centered on the centroid of each voxel. In a given radial orientation, the surface intercepts the radial line at a radial distance equaling to the value of the PDF evaluated at a radial distance *R*. Similar visualization technique was implemented by Özarslan et al (24). Mathematically, a PDF glyph of a given PDF $p(\mathbf{r})$ is a surface defined as

$$glyph = \{\xi : \xi = p(|\mathbf{r}| = R)\hat{\mathbf{r}}\} \ . \tag{6}$$

Here, ξ is the value of probability density function evaluated at a given radial distance and $\hat{\mathbf{r}}$ is a unitless vector along the radial direction. In order to capture the shape of the PDF, *R* should

be large enough. We have found an empirical good value of $R=3\sqrt{2\lambda_1(\Delta-\frac{1}{3}\delta)}$ where λ_1 is the largest eigenvalue of the second-order diffusion tensor. We note that the surface defined by Eq. [6] is different from the isosurface defined in the original GDTI-HOT paper (11). The glyph defined by Eq. [6] guarantees a closed surface while an isosurface, on the other hand, does not.

Validation Studies

Although there is no direct method for validating a diffusion imaging technique *in vivo* without the knowledge of the underlying neural structure and its intrinsic diffusion property, simulation and phantom studies has been usually used for the purpose of validation. Previous simulation studies have shown that GDTI-HOT can measure higher order diffusion tensors and reconstruct the underlying simple fiber structures accurately (12). In this paper, we are interested in establishing HOT as a meaningful *in vivo* measure of non-Gaussian diffusion in the sense that the measurement is reproducible and the information is consistent with existing techniques and with known anatomical structures. For that purpose, we used the bootstrapping technique (25) to evaluate the variability of the measured HOT. Furthermore, we acquired a set of high-resolution (in-plane resolution of 390×390 μm^2) DTI results that illustrated fine details of white matter fibers. Such high-resolution fiber structure were used to verify the GDTI-HOT results obtained on lower resolution images where most voxels are likely to contain multiple fiber pools due to their low spatial resolution and partial volume effect.

Reproducibility studies with bootstrap (gradients, b)—The bootstrap method is a statistical method for assessing the accuracy of sample estimates. This technique allows estimation of the sample distribution of almost any statistic. Given the time-consuming nature of diffusion MRI, bootstrap has gained some popularity in studying the accuracy of diffusion measurements (26,27). In this study, a total of 21 diffusion directions plus a non-diffusion weighted image were acquired seven times. In other words, a total of 154 images were acquired for each slice. In the bootstrap analysis, each set of bootstrap samples contains all 21 directions. For each direction, three images were drawn randomly with replacement (27). In addition, 3 non-diffusion weighted images were also drawn randomly with replacement. In total, there are 66 images in each set of bootstrap samples. For each set of samples, HOT up to order 4 were estimated using the GDTI-HOT model; the regular second-order diffusion tensor was also estimated using the DTI model. This bootstrap process was repeated 10,000 times and the distribution of tensor elements was calculated.

Comparison with High Resolution DTI—The multi-modal fiber structure observed with GDTI-HOT at low spatial resolution can be also verified with high-resolution DTI studies. Because of the limited spatial resolution of diffusion-weighted images, partial volume effect can contribute to the complex fiber structure observed by GDTI-HOT. Although one would like to reduce such partial volume effect in mapping the neural fiber structure, on the other hand, the partial volume effect provides the possibility to verify the structure observed by GDTI-HOT. With high-resolution DTI, one is able to differentiate a number of fiber pools in areas of fiber merging that one otherwise will not be able to distinguish at lower resolution. These merging fibers appear within one voxel in the low-resolution images used in GDTI-HOT such that the structures observed with GDTI-HOT can be cross-validated with the high-resolution DTI results.

High-resolution *in vivo* DTI with an in-plane resolution of 390μm were obtained using the SNAILS technique on the same volunteer as in the GDTI-HOT study. This in-plane resolution represents one of the highest spatial resolutions that have been achieved *in vivo* on a human brain. The scan parameters were: FOV = 192mm, slice thickness = 6mm, number of slices =

10, TR = 2.5s, TE = 76ms, bandwidth (BW) = 125 kHz, matrix size =512×512, number of averages = 2. A total of 64 interleaves of variable-density spirals were used to collect **k**-space data. Diffusion-weighted images were acquired on a set of 6 diffusion encoding directions: [1 1 0], [1 0 1], [0 1 1], [1 -1 0], [1 0 -1] and [0 1 -1]. Here [1 1 0] indicates that relative gradient strengths on three axes are: Gx = 1, Gy = 1 and Gz = 0 respectively. The b-value was 650 s/mm^2. The total scan time for this high-resolution DTI study was 74 minutes with four averages.

Results

Consistency of GDTI-HOT with High Resolution Anatomy

Figure 1a shows the reconstructed PDF glyphs on a representative axial slice through the middle of the brain. The PDF glyphs are plotted over the fractional anisotropy (FA) gray-scale maps on a voxel-by-voxel basis. Figure 1b shows an enlarged region of interest (ROI) in the anterior portion of the brain section that contains the genu of corpus callosum (gcc), the white matter fiber merging area of the gcc, the forceps minor and the anterior corona radiata (left side of the image), and the merging area of the gcc and the corticopontine track (right side of the image). Similarly, Figure 1c shows a zoomed-in ROI of the posterior portion that contains the splenium of corpus callosum (scc), the white matter fiber merging area of the scc, the forceps major and the posterior corona radiata (left side of the image), and the merging area of the scc and the corticopontine track (right side of the image). In the corpus callosum, the PDF glyphs have an elongated shape indicating high probability of diffusion along the white matter fibers, which is consistent with the underlying tissue structure. In the fiber merging areas, the FA is typically low. For example, the FA in the merging area of gcc, the forceps minor and the anterior corona radiata has a value of 0.101 on average while the FA within the gcc is typically 0.520. Nevertheless, the PDF glyphs exhibit a clear non-Gaussian shape within these areas, indicating a multi-modal diffusion pattern that is consistent with the fact that multiple fiber bundles with different orientations coexist within one voxel.

In order to illustrate the detailed fiber structure that is not shown in the low resolution images acquired in the GDTI-HOT protocol, Figure 2 shows the high resolution fiber system with an in-plane resolution of 390×390 μm^2. Figure 2a displays the FA map. Figure 2b displays the color-coded FA map. Figure 2c displays a myelin stained brain section in a similar location obtained from the Yakovlev collection (National Museum of Health and Medicine, Washington, DC). Figure 2d, e & f highlight an enlarged ROI of the FA map, the color-coded FA map and the brain section respectively of a FOV that contains the internal capsule. The high resolution photo illustrates a layered substructure of the internal capsule (Figure 2f). The internal capsule shown in the FA maps (Figure 2d and 2e) demonstrates a structure strikingly similar to that shown in the Yakovlev photo. In addition, the color-coded FA map shows that the fiber in the internal capsule in that particular slice runs in the direction of superior-inferior as indicated by the blue color.

The in-plane spatial resolution of images acquired in the GDTI-HOT protocol is 64 times lower compared to that of the high resolution DTI protocol. As a result, more complex fiber structures can not be revealed anatomically in the low resolution diffusion weighted image or by the DTI results computed based on these low resolution images. Figure 3 compares the PDF glyphs constructed using GDTI-HOT to those using DTI in a FOV containing the fiber merging area of the scc, the forceps major and the posterior corona radiata in the posterior left portion of the slice. Figure 3a shows the corresponding high resolution color-coded FA map obtained in the high resolution DTI protocol. Figure 3b shows the PDF glyphs from GDTI-HOT and Figure 3c shows the PDF glyphs from DTI. Both PDF glyphs are computed using the same low resolution data set acquired with the GDTI-HOT protocol. The rectangular box and the square box in the images highlight two ROI that contain fiber bundles of different orientations. The rectangular box contains two major fiber bundles (Figure 3a): posterior corona radiata (red)

and the superior longitudinal fasciculus (blue). In the low resolution image, one voxel within this box contains both groups of fibers which are revealed by the PDF glyphs reconstructed by GDTI-HOT (Figure 3b). However, such structure is not present in the PDF glyphs reconstructed by DTI (Figure 3c). In fact, the orientation of the PDF glyphs from DTI does not correspond to either of this fiber bundles. Similar observation is seen in the square box that contains both the cingulum and parts of the scc. While the GDTI-HOT glyph shows the orientation of both the cingulum and the scc (Figure 3b), the DTI glyph shows an orientation that deviates from both fiber bundles (Figure 3c). In summary, the number of distinct fiber populations observed for the voxels within these two boxes agrees between the GDTI glyphs and the high-resolution scan. The differences between the orientations are calculated to be within ±5.4°.

The proposed protocol also allows the calculation of the sixth order tensor. However, the sixth-order approximation is likely more susceptible to noise and image artifacts with the increased number of unknowns (49 for the sixth-order approximation and 21 for the fourth-order approximation). Figure 4 shows a comparison of the PDF glyphs from the fourth- and the sixth-order approximation. We observe that the orientations of major fiber bundles mostly agree while the sixth-order approximation appears to demonstrate a sharper angular separation.

Reproducibility of HOT by Bootstrapping

Figure 5 plots the bootstrap distribution of tensor elements for a fiber-crossing voxel within the gcc, the forceps minor and the anterior corona radiata. Figure 5a–f plots the distribution of the diffusion tensor elements calculated by both GDTI-HOT and DTI. Figure 5g–l plots the distribution of the fourth-order tensor elements calculated by GDTI-HOT. Table 1 lists the numerical values of their mean and standard deviation. As another example, Table 1 also lists the mean and standard deviation of the tensor elements for a voxel within the gcc, although the distribution for this voxel is not plotted. In calculating the tensor elements, only data acquired with b = 500 s/mm^2 were used for DTI. Higher b-values were not used for DTI calculation to eliminate the bias caused by non-monoexponential signal decay. In comparison, Figure 5a–f shows that the standard deviation of the second order tensor of GDTI-HOT is in general smaller than that of DTI, which can be attributed to the improved accuracy of the GDTI-HOT diffusion model. For example, for the multiple fibers example in Table 1, the standard deviation for the non-trivial second order tensor elements as a percentage of the mean is 3.7% on average for DTI and 2.3% for GDTI-HOT; for the single fiber bundle example, it is 3.1% for DTI and 3.0% for GDTI-HOT.

Discussions

We have demonstrated an *in vivo* implementation of GDTI-HOT using higher order tensors on a human brain. A protocol that used four b-values and 21 diffusion directions with whole brain coverage was used to acquire the images. Second-order, fourth-order and sixth-order diffusion tensors were estimated. For clinical feasibility, however, the primary purpose of this protocol is to provide a reliable measurement of tensors up to the fourth order. The PDF glyphs reconstructed using these higher order tensors revealed the underlying fiber structure within one voxel. These structures were verified by the fiber structure acquired at a 64-times higher resolution. In addition, bootstrap studies have shown that the measurement of the higher order tensors with GDTI-HOT is reproducible with a variance less than 5% for non-trivial tensor elements.

The validation of diffusion models, especially the validation of models that aim to improve the angular resolution of neural fiber structures, has been challenging. The lack of other established *in vivo* imaging techniques has made it difficult to cross reference the diffusion imaging results for *in vivo* brain imaging. Instead, computer simulations, diffusion phantoms with simple

structures, and in vitro tissue samples have been used as alternatives. For example, Monte Carlo simulation has been used to simulate non-Gaussian diffusion in restricted environments and to validate the accuracy of higher order diffusion tensors in characterizing such diffusion processes (12,28). There is also a growing interest in constructing physical diffusion phantoms that mimic the hindered diffusion environment observed in human brain (6,29). Furthermore, experiments have also been attempted on in vitro tissue samples with relatively simple and known fiber structure (7,30). In this study, we have attempted to show, *in vivo*, that fiber structures obtained with GDTI-HOT on human brain are consistent with high resolution fiber anatomy. Although this *in vivo* validation is not exhaustive and the validation still relies on the accuracy of high-resolution DTI in obtaining major fiber orientations, this study demonstrates that GDTI-HOT has the capability to reveal fiber structures that are otherwise unobtainable at the same spatial resolution with DTI.

Besides demonstrating the consistency of GDTI-HOT with high resolution fiber anatomy, we have also studied the reproducibility of the GDTI-HOT in measuring higher order statistics of diffusion processes *in vivo* by a bootstrap technique. Bootstrap analysis is a widely used technique for assessing the accuracy of statistical estimation. A great advantage of bootstrapping is its applicability to limited amount of samples and its independence of the actual statistical distribution of the estimation. In the context of DTI, bootstrapping has been shown to be useful in studying the distribution of the measured diffusion tensor and the variation of fiber orientation obtained by DTI fiber tractography (26). In this study, with bootstrap analysis, we are able to evaluate the distribution of the estimated higher order diffusion tensor elements. The results indicate that the measurement of higher order diffusion tensors can be reproduced with a variance less than 5%. It should be noted that there are a number of variations of bootstrap analysis (31); here we applied the original bootstrap technique (25,27). Our focus is not the comparison of these techniques which has been considered in previous studies (31). We have also limited our study to analyzing the distribution of the tensor elements rather than the distribution of the tensor objects themselves. From the bootstrap analysis, the distribution of higher-order tensor components appears normal. In fact, we expect the distribution of higher-order tensor components to be the same as the second-order tensor components because all tensor components are linearly combined in the least-squares estimation. The statistical distribution of the second-order diffusion tensor has been considered by Basser et al (32). In principle, normal distribution of the higher-order tensors can also be defined accordingly.

A limitation in the study of the consistency is the reliance on the quality and the accuracy of high resolution DTI. By using the fiber structures obtained by high resolution DTI as a reference, we have assumed that these fiber structures reflect the actual fiber structure. Even at a resolution of 390μm, this assumption cannot be expected to hold for all neural fiber structures given that the average size of axons are on the order of 10μm. However, this assumption is reasonable for large fiber bundles such as the gcc, the scc, the forceps minor, the forceps major etc. The recent development of parallel imaging (33) and multi-shot DWI techniques (20,34) including the SNAILS has allowed us to significantly improve the spatial resolution of diffusion-weighted images. In fact, the 390μm resolution is among the highest resolution has been achieved *in vivo*. In addition, the application of multi-shot techniques was crucial in dramatically reducing the geometric distortion that is common in single-shot DWI. With the relatively large number of images (84 images for the GDTI-HOT protocol and 588 images for the bootstrap analysis) required for the estimation of higher order tensors, it is critical that diffusion weighted images at diffusion encoding direction do not suffer from different geometric distortions. Such type of diffusion-gradient dependent distortion is common in the single-shot EPI DWI sequence that is commonly used on clinical scanners. With shorter readout time and radial symmetric sampling, SNAILS DWI was able to avoid this kind of distortion.

An important implication of this study is that higher order tensor statistics can significantly improve the angular resolution of the multiple fiber bundles within one voxel and consequently should be able to improve the accuracy of fiber tractography. We have shown that with limited spatial resolution, a second-order diffusion tensor alone not only fails to resolve multiple fiber orientations but also fails to identify a correct orientation among all existing orientations (Figure 3c). In addition, the reduced FA within fiber merging area is also problematic for DTI based tractography. We expect that by incorporating higher order information, GDTI-HOT improves fiber tractography especially in regions where multi-modal diffusion exists and the second order model fails.

The *in vivo* GDTI-HOT study also leads us to believe that, while much emphasis in the literature of fiber tractography has been focused on developing new tracking algorithms, improvement to the quality of fiber tracking requires both improvement to the spatial resolution of diffusion-weighted images and improvement to the angular resolution of the PDF of diffusion process. Improving spatial resolution requires further development of image acquisition techniques including parallel imaging and multi-shot acquisition. Fundamentally improving angular resolution, on the other hand, requires the statistical information of non-Gaussian diffusion which is provided by higher order tensor statistics. Such information cannot be obtained by simply increasing the spatial resolution as evidenced by reports of restricted diffusion observed within intracellular space (35). Therefore, a combination of higher spatial resolution and increased characterization of the PDF is necessary to improve our understanding of the neural structure.

More importantly, these higher order contrasts provide additional quantification of tissue integrity. In a deceased state, such as stroke and trauma, cellular damages in tissue could alter the diffusion property and possibly change the higher order contrast as a consequence of reduced non-Gaussian diffusion. Further exploration may show the relevance of higher order contrasts as novel biomarkers.

Conclusions

In conclusion, we have demonstrated *in vivo* implementation of GDTI-HOT of higher order tensor statistics. We have shown that *in vivo* measurement of HOT can be achieved *in vivo* on a clinical scanner using a protocol with four b-values and 21 directions. By comparing the orientation of the PDF glyphs to higher resolution fiber structure, we are able to show that the GDTI-HOT has the capability to resolve multiple fiber orientations within one voxel. Using bootstrap analysis, we have also shown that higher order tensor statistics can be reliably reproduced using GDTI-HOT with a variance that is smaller than that of DTI.

Acknowledgments

The study is supported in part by NIH Pathway to Independence Award (NIH-5K99EB007182), the Lucas Foundation, and the Center of Advanced MR Technology of Stanford (NCRR P41RR09784). SCM was supported by the German Academic Exchange Service (“DAAD-Doktorandenstipendium”).

References

1. Moseley ME, Kucharczyk J, Mintorovitch J, Cohen Y, Kurhanewicz J, Derugin N, Asgari H, Norman D. Diffusion-weighted MR imaging of acute stroke: correlation with T2-weighted and magnetic susceptibility-enhanced MR imaging in cats. AJNR Am J Neuroradiol 1990;11(3):423–429. [PubMed: 2161612]
2. Basser PJ, Mattiello J, LeBihan D. MR diffusion tensor spectroscopy and imaging. Biophys J 1994;66 (1):259–267. [PubMed: 8130344]

3. Basser PJ. Relationships between diffusion tensor and q-space MRI. Magn Reson Med 2002;47(2): 392–397. [PubMed: 11810685]
4. Assaf Y, Cohen Y. Structural information in neuronal tissue as revealed by q-space diffusion NMR spectroscopy of metabolites in bovine optic nerve. NMR Biomed 1999;12(6):335–344. [PubMed: 10516615]
5. King MD, Houseman J, Roussel SA, van Bruggen N, Williams SR, Gadian DG. q-Space imaging of the brain. Magn Reson Med 1994;32(6):707–713. [PubMed: 7869892]
6. Lin CP, Wedeen VJ, Chen JH, Yao C, Tseng WY. Validation of diffusion spectrum magnetic resonance imaging with manganese-enhanced rat optic tracts and ex vivo phantoms. Neuroimage 2003;19(3): 482–495. [PubMed: 12880782]
7. Wedeen VJ, Wang RP, Schmahmann JD, Benner T, Tseng WY, Dai G, Pandya DN, Hagmann P, D'Arceuil H, de Crespigny AJ. Diffusion spectrum magnetic resonance imaging (DSI) tractography of crossing fibers. Neuroimage. 2008
8. Frank LR. Anisotropy in high angular resolution diffusion-weighted MRI. Magn Reson Med 2001;45 (6):935–939. [PubMed: 11378869]
9. Tuch DS, Reese TG, Wiegell MR, Makris N, Belliveau JW, Wedeen VJ. High angular resolution diffusion imaging reveals intravoxel white matter fiber heterogeneity. Magn Reson Med 2002;48(4): 577–582. [PubMed: 12353272]
10. Tuch DS. Q-ball imaging. Magn Reson Med 2004;52(6):1358–1372. [PubMed: 15562495]
11. Liu C, Bammer R, ME M. Generalized diffusion tensor imaging (GDTI): a method for characterizing and imaging diffusion anisotropy caused by non-gaussian diffusion. Israel J Chem 2003;43:145–154.
12. Liu C, Bammer R, Acar B, Moseley ME. Characterizing non-Gaussian diffusion by using generalized diffusion tensors. Magn Reson Med 2004;51(5):924–937. [PubMed: 15122674]
13. Ozarslan E, Mareci TH. Generalized diffusion tensor imaging and analytical relationships between diffusion tensor imaging and high angular resolution diffusion imaging. Magn Reson Med 2003;50 (5):955–965. [PubMed: 14587006]
14. Liu C, Bammer R, Moseley ME. Limitations of apparent diffusion coefficient-based models in characterizing non-gaussian diffusion. Magn Reson Med 2005;54(2):419–428. [PubMed: 16032684]
15. McCullagh, P. Tensor Methods in Statistics. New York: Chapman and Hall; 1987.
16. Jensen JH, Helpern JA, Ramani A, Lu H, Kaczynski K. Diffusional kurtosis imaging: the quantification of non-gaussian water diffusion by means of magnetic resonance imaging. Magn Reson Med 2005;53(6):1432–1440. [PubMed: 15906300]
17. Hui ES, Cheung MM, Qi L, Wu EX. Towards better MR characterization of neural tissues using directional diffusion kurtosis analysis. Neuroimage 2008;42(1):122–134. [PubMed: 18524628]
18. Frank LR. Characterization of anisotropy in high angular resolution diffusion-weighted MRI. Magn Reson Med 2002;47(6):1083–1099. [PubMed: 12111955]
19. Zucker U, Schulz H. Statistical approaches for the treatment of anharmonic motion in crystals. I. A comparison of the most frequently used formalisms of anharmonic thermal vibrations. Acta Crystallographica Section A 1982;38(5):563–568.
20. Liu C, Bammer R, Kim DH, Moseley ME. Self-navigated interleaved spiral (SNAILS): application to high-resolution diffusion tensor imaging. Magn Reson Med 2004;52(6):1388–1396. [PubMed: 15562493]
21. Jones DK, Horsfield MA, Simmons A. Optimal strategies for measuring diffusion in anisotropic systems by magnetic resonance imaging. Magn Reson Med 1999;42(3):515–525. [PubMed: 10467296]
22. Mang SC, Gembris D, Grodd W, Klose U. Comparison Of Gradient Encoding Directions For Higher Order Tensor Diffusion Data. Magn Reson Med. 2008 in press.
23. Liu C, Moseley ME, Bammer R. Simultaneous phase correction and SENSE reconstruction for navigated multi-shot DWI with non-cartesian k-space sampling. Magn Reson Med 2005;54(6):1412–1422. [PubMed: 16276497]
24. Ozarslan E, Shepherd TM, Vemuri BC, Blackband SJ, Mareci TH. Resolution of complex tissue microarchitecture using the diffusion orientation transform (DOT). Neuroimage 2006;31(3):1086–1103. [PubMed: 16546404]

25. Efron B. Bootstrap Methods: Another Look at the Jackknife. The Annals of Statistics 1979;7(1):1–26.
26. Jones DK. Determining and visualizing uncertainty in estimates of fiber orientation from diffusion tensor MRI. Magn Reson Med 2003;49(1):7–12. [PubMed: 12509814]
27. Pajevic S, Basser PJ. Parametric and non-parametric statistical analysis of DT-MRI data. J Magn Reson 2003;161(1):1–14. [PubMed: 12660106]
28. Coremans J, Luypaert R, Verhelle F, Stadnik T, Osteaux M. A method for myelin fiber orientation mapping using diffusion-weighted MR images. Magn Reson Imaging 1994;12(3):443–454. [PubMed: 8007774]
29. Perrin M, Poupon C, Rieul B, Leroux P, Constantinesco A, Mangin JF, Lebihan D. Validation of q-ball imaging with a diffusion fibre-crossing phantom on a clinical scanner. Philos Trans R Soc Lond B Biol Sci 2005;360(1457):881–891. [PubMed: 16087433]
30. Assaf Y, Mayk A, Cohen Y. Displacement imaging of spinal cord using q-space diffusion-weighted MRI. Magn Reson Med 2000;44(5):713–722. [PubMed: 11064406]
31. Chung S, Lu Y, Henry RG. Comparison of bootstrap approaches for estimation of uncertainties of DTI parameters. Neuroimage 2006;33(2):531–541. [PubMed: 16938472]
32. Basser PJ, Pajevic S. A normal distribution for tensor-valued random variables: applications to diffusion tensor MRI. IEEE Trans Med Imaging 2003;22(7):785–794. [PubMed: 12906233]
33. Pruessmann KP, Weiger M, Bornert P, Boesiger P. Advances in sensitivity encoding with arbitrary k-space trajectories. Magn Reson Med 2001;46(4):638–651. [PubMed: 11590639]
34. Pipe JG, Farthing VG, Forbes KP. Multishot diffusion-weighted FSE using PROPELLER MRI. Magn Reson Med 2002;47(1):42–52. [PubMed: 11754441]
35. Sehy JV, Ackerman JJ, Neil JJ. Evidence that both fast and slow water ADC components arise from intracellular space. Magn Reson Med 2002;48(5):765–770. [PubMed: 12417990]

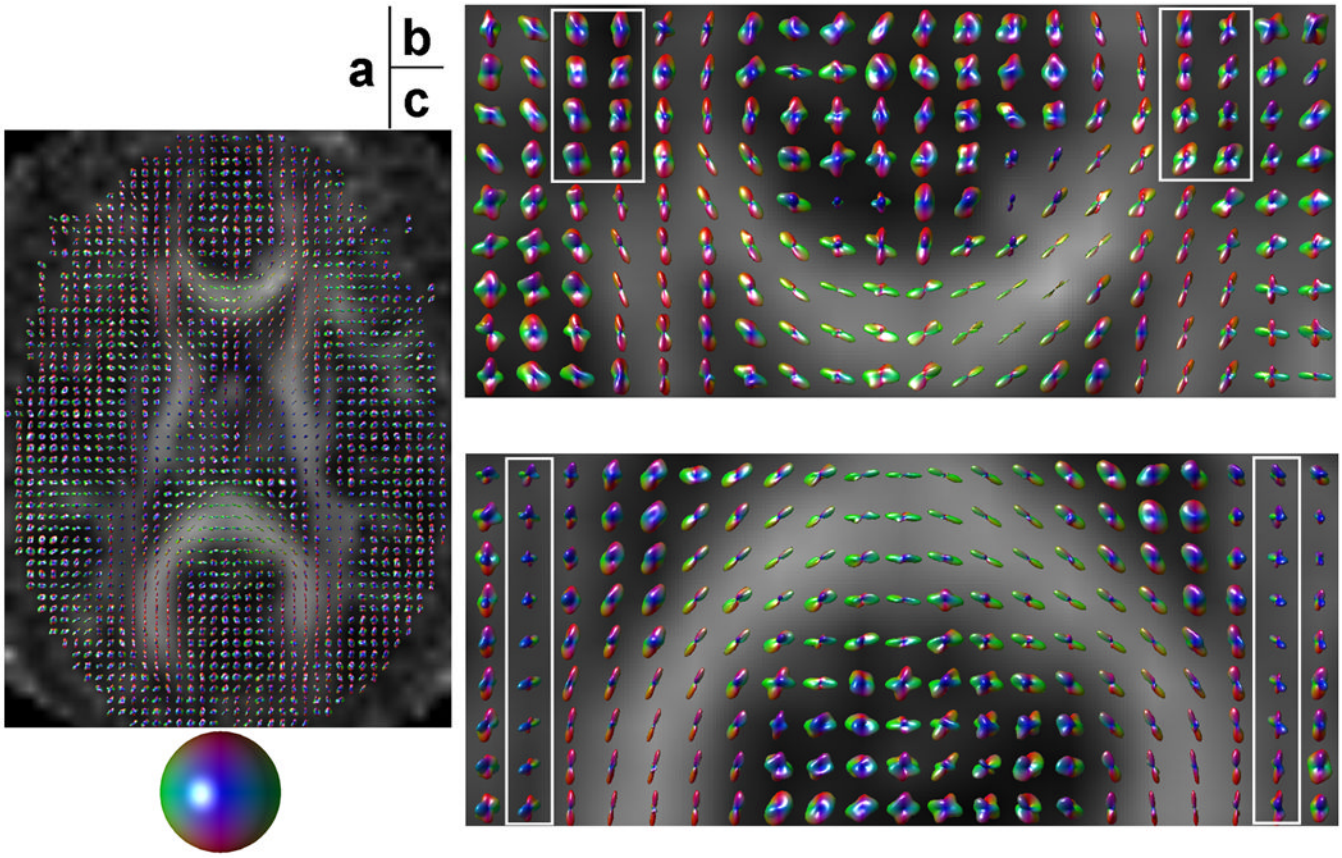

Figure 1.

Color-coded 3D PDF glyphs reconstructed with GDTI-HOT plotted over gray-scale FA maps. The 3D color coding scheme is illustrated in the lower left corner of the image. Red represents the direction of anterior-posterior; green represents the direction of left-right; blue represents the direction of superior-inferior. (a) PDF glyphs on a representative axial slice through the middle of the brain. The PDF glyphs are plotted over the FA maps on a voxel-by-voxel basis. (b) An enlarged FOV in the anterior portion of the brain section that contains the genu of corpus callosum and some white matter fiber merging areas (two areas are highlighted in white rectangular boxes). (c) A posterior portion containing the splenium of corpus callosum and some white matter fiber merging areas (two areas are highlighted in white rectangular boxes). In the corpus callosum, the PDF glyphs are aligned with the fiber bundle. In the areas of fiber merging, FA is low but PDF glyphs points out multiple fiber orientations. The single voxel contained in the red square box in (b) and (c) is used for the analysis in Figure 5 and Table 1.

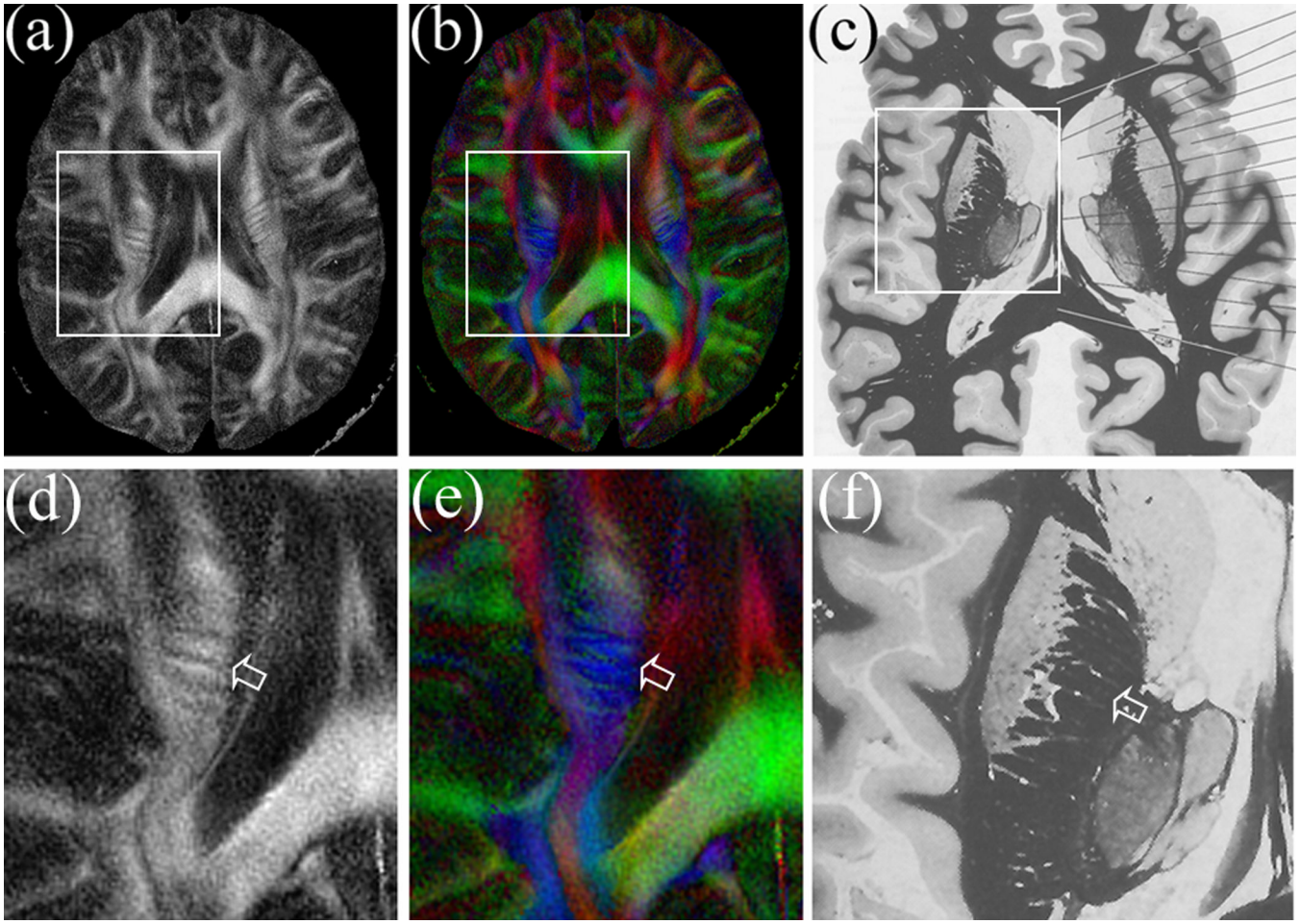

Figure 2.
High resolution SNAILS DTI with an in-plane resolution of 390×390 μm^2. (a) FA map. (b) Color-coded FA map with red representing the direction of anterior-posterior, green representing the direction of left-right and blue representing the direction of superior-inferior. (c) Myelin stained brain section in a similar location obtained from the Yakovlev collection (National Museum of Health and Medicine, Washington, DC). (d, e & f) An enlarged ROI indicated by the rectangular boxes in a, b and c showing the FA map, the color-coded FA map and the brain section respectively. Substructures of the internal capsule are shown clearly in the FA maps that match the tissue morphology (arrow).

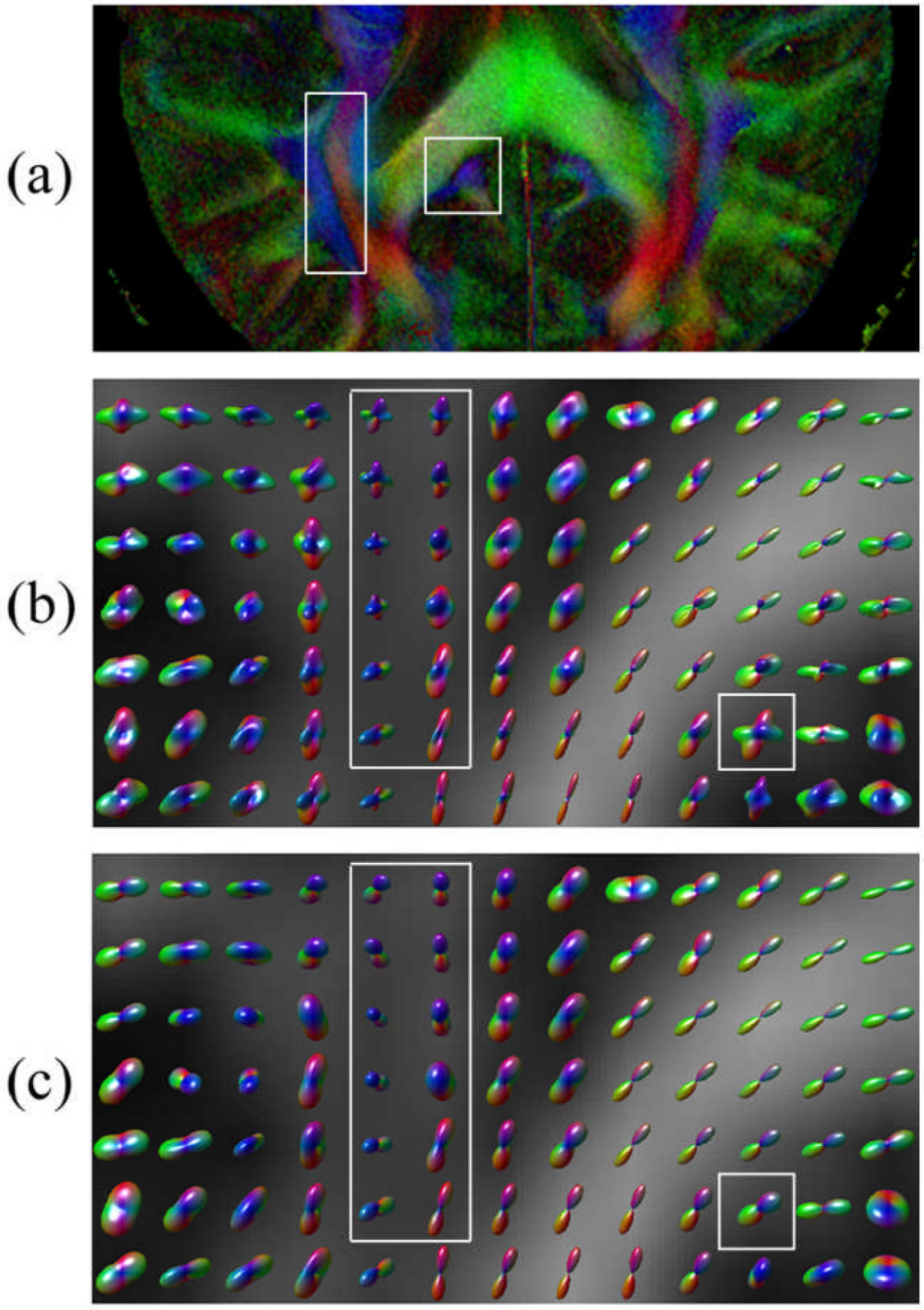

Figure 3.

Comparison of the PDF glyphs constructed using GDTI-HOT and DTI. Two ROI (the rectangular and the square box) are highlighted for comparison. (a) An anterior portion of the high resolution color-coded FA map shown in Figure 2b. The rectangular box and the square box in the images highlight two ROI that contain fiber bundles of different orientations. The rectangular box on the left contains two major fiber bundles: posterior corona radiata (red) and the superior longitudinal fasciculus (blue). The square box contains cingulum and part of splenium corpus callosum. (b) PDF glyphs constructed by GDTI-HOT. (c) Corresponding PDF glyphs constructed by DTI. The GDTI-HOT glyphs depict multiple fiber orientations within

these two boxes that match the fiber bundles shown in (a). In comparison, DTI glyphs are unidirectional.

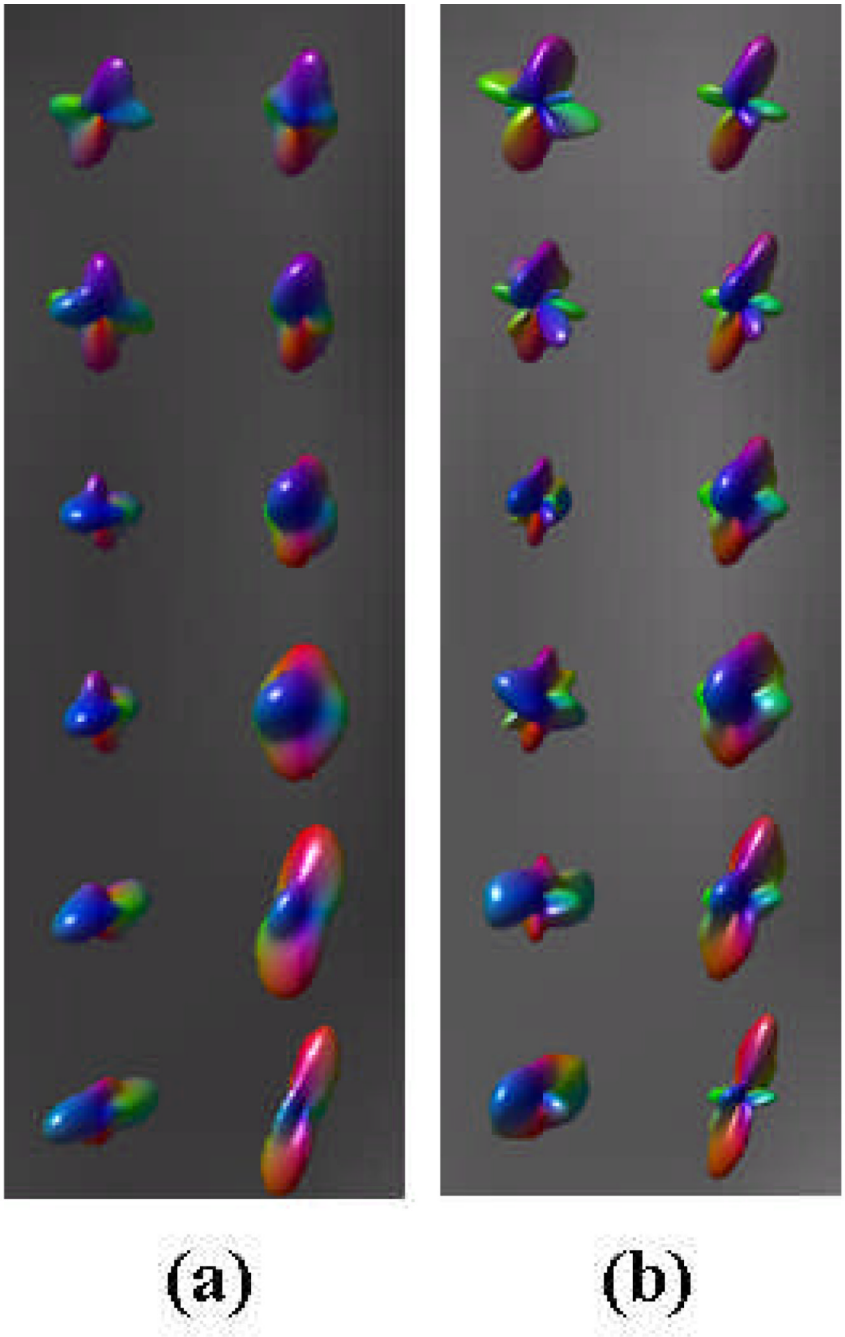

Figure 4.
A comparison of PDF glyphs reconstructed with the fourth-order and the sixth-order approximation for voxels inside the rectangular ROI shown in Figure 3. (a) Fourth-order approximation; (b) Sixth-order approximation.

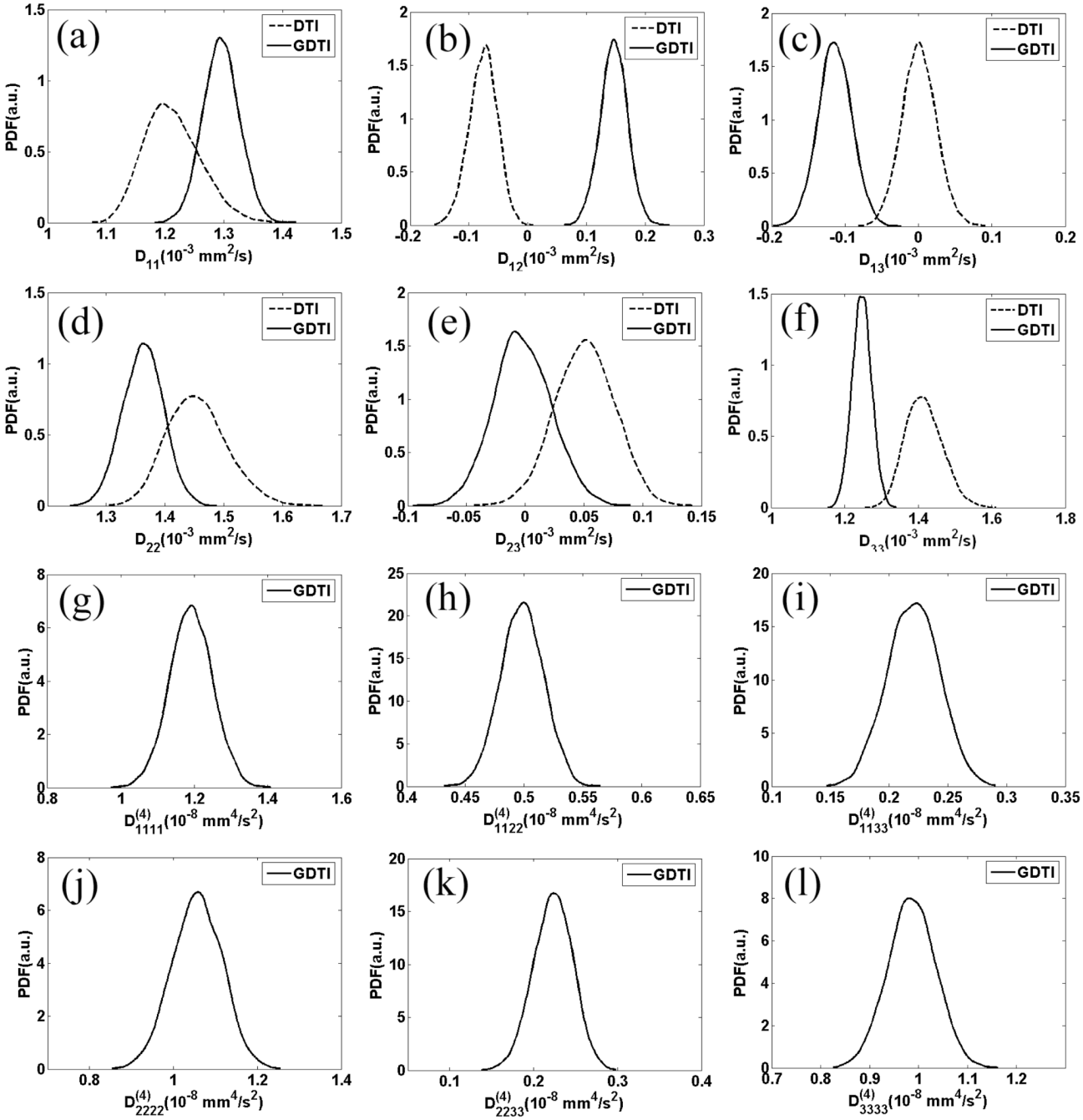

Figure 5.

The distribution of the estimated second-order tensor elements estimated by bootstrap analysis. The distribution was obtained for a fiber-crossing voxel within the genu of corpus callosum, the forceps minor and the anterior corona radiata. The voxel is in the red square box in the upper left corner of Figure 1b. (a–f) The distribution of the second-order tensor elements of both DTI and GDTI-HOT. (g–l) The distribution of the fourth-order tensor elements of GDTI-HOT. The fourth-order tensor does not exist for DTI, therefore it was not plotted here.

Table 1

Bootstrap mean and standard deviation of tensor elements estimated by DTI and GDTI-HOT for the two voxels shown in Figure 1b and 1c in red square boxes. The voxel shown in Figure 1b that contains multiple fiber bundles of different orientations is the same voxel as that used in Figure 4. The voxel shown in Figure 1c is located within the splenium of corpus callosum. In DTI analysis, although multiple b-values are available, tensor elements shown are computed with b = 500 s/mm^2. This selection of b-value provides a more meaningful comparison with the second order tensor estimated with GDTI-HOT.

	Multiple Fibers (voxel in Fig. 1b)				**Single Fibers (voxel in Fig. 1c)**			
	DTI (b = 500 s/mm^2)		**GDTI-HOT**		**DTI (b = 500 s/mm^2)**		**GDTI-HOT**	
	Mean	**Std Dev**	**Mean**	**Std Dev**	**Mean**	**Std Dev**	**Mean**	**Std Dev**
Units (2^{nd} order)	10^{-3} mm^2/s							
$D^{(2)}_{11}$	1.21	0.05	1.30	0.03	1.00	0.05	1.10	0.04
$D^{(2)}_{12}$	−0.08	0.03	0.15	0.02	−0.34	0.04	−0.16	0.05
$D^{(2)}_{13}$	0.0	0.02	−0.11	0.02	0.25	0.03	0.24	0.04
$D^{(2)}_{22}$	1.45	0.05	1.38	0.03	1.40	0.05	1.31	0.03
$D^{(2)}_{23}$	0.05	0.03	−0.002	0.02	−0.007	0.03	−0.05	0.04
$D^{(2)}_{33}$	1.42	0.05	1.25	0.03	1.70	0.06	1.61	0.05
Units (4^{th} order)	10^{-8} mm^4/s^2							
$D^{(4)}_{1111}$	-	-	1.19	0.06	-	-	0.82	0.06
$D^{(4)}_{1112}$	-	-	0.27	0.03	-	-	−0.12	0.05
$D^{(4)}_{1113}$	-	-	−0.09	0.03	-	-	0.02	0.06

	Multiple Fibers (voxel in Fig. 1b)				Single Fibers (voxel in Fig. 1c)			
	DTI ($b = 500$ s/mm^2)		GDTI-HOT		DTI ($b = 500$ s/mm^2)		GDTI-HOT	
	Mean	Std Dev	Mean	Std Dev	Mean	Std Dev	Mean	Std Dev
$D^{(4)}_{1122}$	-	-	0.51	0.02	-	-	0.52	0.04
$D^{(4)}_{1123}$	-	-	−0.15	0.01	-	-	0.01	0.02
$D^{(4)}_{1133}$	-	-	0.22	0.02	-	-	0.36	0.04
$D^{(4)}_{1222}$	-	-	0.09	0.03	-	-	0.19	0.06
$D^{(4)}_{1223}$	-	-	−0.03	0.01	-	-	−0.03	0.02
$D^{(4)}_{1233}$	-	-	0.01	0.02	-	-	0.078	0.03
$D^{(4)}_{1333}$	-	-	−0.09	0.03	-	-	0.12	0.05
$D^{(4)}_{2222}$	-	-	1.04	0.06	-	-	0.20	0.03
$D^{(4)}_{2223}$	-	-	−0.05	0.03	-	-	0.060	0.05
$D^{(4)}_{2233}$	-	-	0.22	0.02	-	-	0.73	0.04
$D^{(4)}_{2333}$	-	-	0.10	0.03	-	-	−0.14	0.04
$D^{(4)}_{3333}$	-	-	0.99	0.05	-	-	0.86	0.05